JOURNAL OF Materials CHEMISTRY

Extended defect structures in zinc oxide doped with iron and indium

Tom Hörlin,*[a] Gunnar Svensson[b] and Eva Olsson[c]†

[a] *Department of Inorganic Chemistry, Stockholm University, SE-106 91 Stockholm, Sweden. E-mail: tom@inorg.su.se*
[b] *Department of Structural Chemistry, Stockholm University, SE-106 91 Stockholm, Sweden*
[c] *Department of Physics, Chalmers University of Technology and Gothenburg University, SE-41296 Gothenburg, Sweden*

Received 8th July 1998, Accepted 26th August 1998

The effects of iron- and indium oxide doping on the structure and magnetic susceptibility of ZnO have been studied. The nominal compositions were $In_xFe_{2-x}O_3(ZnO)_n$ with $0 \leqslant x \leqslant 1$ and $n = 23$, 48 and 98. Magnetic measurements showed the iron-doped samples to be paramagnetic, with a behaviour indicating antiferromagnetic coupling between the iron ions. HREM studies showed that indium and iron are incorporated as layer defects of two kinds. One type forms cubic close packed (ccp) planes perpendicular to the *c* axis, and the other appears as corrugated layers inserted between the former. The folds in the corrugated layers consist of alternating (114) and ($11\bar{4}$) planes. Analytical transmission electron microscopy studies revealed that indium prefers the ccp layers, whereas iron can be found in both types of defects. Structural models based upon the experimental results are presented.

Introduction

Zinc oxide is one of the most important semiconductors used in large quantities. Although ZnO devices are quite different from components made of *e.g.* silicon and gallium arsenide, there are similarities that can be utilised. Examples are the enhancement of conductivity by doping and the creation of non-linear junctions. The project described in this article was initiated by a study of the possibility of using ZnO as electrode material in the smelting of aluminium.

It is easy to promote the electric conductivity of zinc oxide by doping it with normally trivalent metals. Some of these ions may enter as divalent, with one rather loosely bound electron that may dissociate and participate in *n*-type conduction. Only *n*-conduction has been confirmed in zinc oxide; *p*-conduction has not yet been observed.

It is known[1–3] that the addition of gallium or indium ions enhances the electric conductivity of ZnO, which soon becomes metallic. For gallium a maximum of the conductivity has been observed around 0.4 atom% of the dopant.[3] This result is in agreement with what we have found for both gallium and indium.[4] Iron-doped ZnO stays semiconducting, on the other hand, with a maximum iron content of 0.3–0.5 atom% at 1000 °C. The reason for this is that Fe^{2+} has a higher ionisation energy than In^{2+}. Simultaneous doping with 1 atom% indium and iron does not markedly increase the conductivity at low temperatures, since at this doping level there is enough trivalent iron to trap all loosely bound electrons according to the reaction:[4]

$$In^{2+} + Fe^{3+} \rightarrow In^{3+} + Fe^{2+} \quad (1)$$

If doped ZnO is prepared in air, only a fraction of the trivalent dopant ions will be reduced to divalent. Divalent dopants may substitute for zinc without structural consequences, but the trivalent ions entering ZnO must be accompanied by structural defects such as metal vacancies or other alien structure elements in order to conserve charge neutrality. Sooner or later these defects may start to order in the host structure, eventually leading to new phases.

There have been numerous studies of binary and ternary systems with ZnO and one or two trivalent metal oxides.[2–22] The In_2O_3–ZnO system was first studied by Kasper,[5] who found an homologous series with the general formula $In_2Zn_nO_{3+n}$. Cannard and Tilley[6] later reinvestigated the system using X-ray powder diffraction and transmission electron microscopy. They suggested an intergrowth structure consisting of slabs of wurtzite-type ZnO separated by bixbyite-type layers of In_2O_3. The structures suggested by Cannard and Tilley have recently been confirmed by McCoy *et al.*[7]

The phase compsitions in the In_2O_3–Fe_2O_3–ZnO system have been investigated by Nakamura *et al.*,[9,15] Kimizuka *et al.*[8,10,11] and Siratori and Kimuzuka.[13] They found a number of phases which can be described by the formula $In_xFe_{2-x}O_3(ZnO)_n$ were *n* varies between 1 and 13 and *x* as $0.72 \leqslant x \leqslant 1.00$ for $n = 1$ and as $0 \leqslant x \leqslant 2.0$ for $n = 13$. They suggest that the compounds with $n = 1$–6 and $x = 1$ are isostructural with their lutetium analogues $LuFeO_3(ZnO)_n$, which have been determined by X-ray single-crystal diffraction techniques.[23] The structures consist of wurtzite-type ZnO slabs intergrown with single layers of indium atoms in octahedral cavities formed by cubic close packed oxygen. The iron atoms form a dilute solution in the ZnO slabs. For structural reasons the ZnO tetrahedra have to be connected with their apices to the ccp layers. The ZnO slabs have different polarity on either side of the indium-containing layers. Consequently, an inversion of the polarity must occur within the ZnO slabs between these layers, which can be achieved by a gradual displacement of the metal atoms from one tetrahedron to the neighbouring one *via* the shared triangular face.

HREM studies on $InFeO_3(ZnO)_n$, however, revealed a more complex picture.[19–22] At least for $n \geqslant 6$, wave-like defects were found between the indium oxide layers. EDS spot analysis showed an increased signal from iron in these defects.

In this article we will describe how low concentrations of iron and indium dopant, lower than those reported in the literature, are structurally accommodated in ZnO. We will discuss what structure elements are formed and how are they related to the phases found at higher dopant concentrations, and how this doping influences the magnetic properties of the compounds.

Experimental

Powders of ZnO (Fotofax), Fe_2O_3 (Merck *p.a.*) and In_2O_3 (Aldrich 4N) were milled with SIALON balls in high-density

†Present address: Analytical Materials Physics, The Ångström Laboratory, Uppsala University, Box 534, SE 75121 Uppsala, Sweden.

polyethylene bottles. The powder mixtures were pressed to pellets, which were heated at 1400 °C for 3 days, embedded in loosely packed ZnO powder. After the heating period the furnace was switched off and the door was opened. Earlier work[9] indicates that very long heating periods (weeks) are required to obtain ordered phases. Our dopant (In+Fe) compositions—2, 4 and 8% of the total metal content—were more dilute, so we did not expect to reach complete three-dimensional ordering. The formula can be written as $In_xFe_{2-x}O_3(ZnO)_n$ where $n=98$, 48, 23, and $x=0.0$, 0.5, 1.0. The inner parts of the pellets were used for characterisation. Solid pieces were cut for the magnetic susceptibility measurements and for the electric measurements. Fine powders were ground for X-ray and HREM investigations.

X-Ray powder diffraction patterns were recorded with a focusing camera of Guiner–Hägg type, using Cu-Kα_1 radiation and with silicon added as internal standard ($a=5.431$ Å). The films were evaluated with a scanner system.[24]

For high-resolution electron microscopy studies (HREM) we used a JEOL JEM 200CX operated at 200 kV, capable of 2.4 Å point resolution, and a JEOL JEM 3010 operated at 300 kV, capable of 1.7 Å point resolution; and for the analytical TEM studies a field-emission gun Philips CM200 supertwin microscope operated at 200 kV, equipped with an Oxford LINK ISIS EDX system and a Gatan imaging filter for electron energy loss spectroscopy (EELS) and electron spectroscopy imaging (ESI). For high-resolution and analytical transmission electron microscopy studies, dispersions in *n*-butanol of finely crushed samples were put on perforated carbon films supported by a copper grid.

A model 7000 AC susceptometer from Lake Shore, equipped with a 'Cryodyne' closed-cycle helium refrigerator from CTI Cryogenics, was used for the measurements of magnetic susceptibility. We have also added a computer-controlled differential transformer to the system, because the excellent balance of the pick-up coils at room temperature and moderate frequencies declines at low temperatures and high frequencies, and it is therefore necessary to have a device that can restore the balance when the temperature and frequency vary. The system is controlled by an in-house developed computer program.

The samples were pieces around 0.7 g in weight. The magnetising field (H) ranged from 177 A m^{-1} up to 707 A m^{-1}; the stronger fields were used for samples with less iron. The frequency was 2000 Hz. The temperature was varied from *ca.* 11.3 K up to 320 K. The susceptibilities of the samples were found to be independent of frequency and magnetising field.

Results

X-Ray powder diffraction

All the X-ray powder patterns showed strong lines from a hexagonal unit cell closely similar to that of ZnO. The XRD pattern for the $n=23$ and $x=1.0$ sample is shown in Fig. 1.

(i) The XRD patterns of the $n=98$ and $x=0.0$ samples revealed no additional lines, and only one faint extra line was seen for the $x=0.5$ and 1.0 samples.

(ii) The XRD patterns of all the $n=48$ samples contained the same extra line mentioned above, and for the $x=0.5$ and 1.0 samples of $n=48$, five faint additional extra lines were observed.

(iii) The X-ray powder pattern of the $n=23$, $x=0.0$ sample showed three weak extra lines, and those of the $x=0.5$ and 1.0 samples seven and five weak extra lines, respectively.

The unit cell volume for the ZnO phase in the $n=98$ samples was the same as for undoped ZnO, while it increased for $n=48$ and 23 samples as shown in Fig. 2(*a*). The increase was largest for samples containing both indium and iron. The c/a ratio increased with decreasing n value, but less so for the $x=1.0$ samples, as shown in Fig. 2(*b*). In all samples c/a was less than the ideal value for hcp packing: $c/a=2(2/3)^{1/2}\approx1.630$.

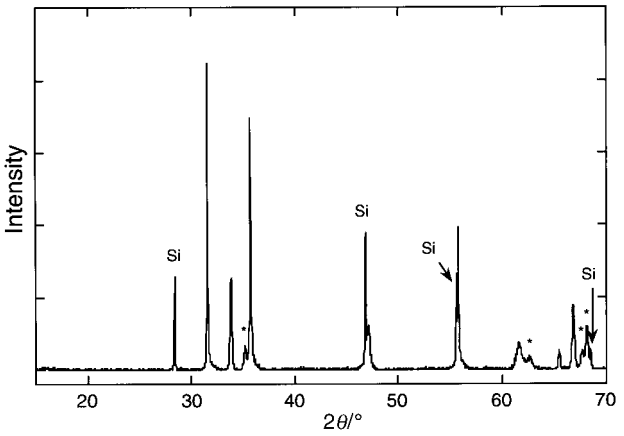

Fig. 1 The XRD pattern for the $n=23$, $x=1$ sample. The additional lines not indexed with a ZnO type unit cell are marked with arrows.

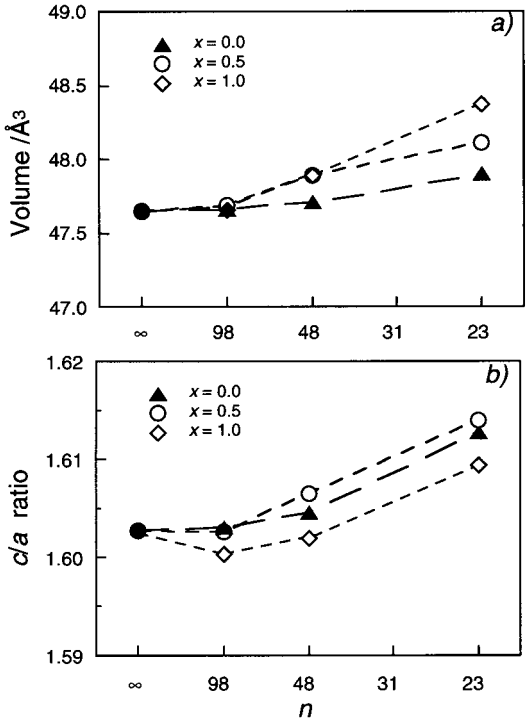

Fig. 2 (*a*) Unit cell volume and (*b*) c/a ratio *versus* $1/n$ and x, for $In_xFe_{2-x}O_3(ZnO)_n$, $n=23$, 48, 98, ∞ and $x=0$, 0.5, 1.0.

HRTEM studies

We first looked for crystal fragments oriented along a [100] direction of ZnO, since the two shortest projected distances between zinc atoms (2.82 and 2.77 Å) in the corresponding $(\bar{2}10)$-projection are well within the resolution of our HRTEM. [The difference between these distances is due to a slight distortion of the tetrahedra ($c/a\neq1.630$).] We then looked parallel to possible planar defects perpendicular to the c-axis, such as those reported by Uchida *et al.*[21] Fig. 3 shows the HREM image and the corresponding electron diffraction pattern taken along [100] of a crystal found in a sample of the nominal composition $InFeO_3(ZnO)_{23}$. A magnification of the edge is shown in Fig. 3(*c*). In the images we see two types of irregularities in the ZnO sructure, similar to those reported by Uchida *et al.*[21] One type is a sharp uninterrupted defect, unwrinkled and perpendicular to the c-axis. Most probably these defects are extended in depth, forming layers parallel to

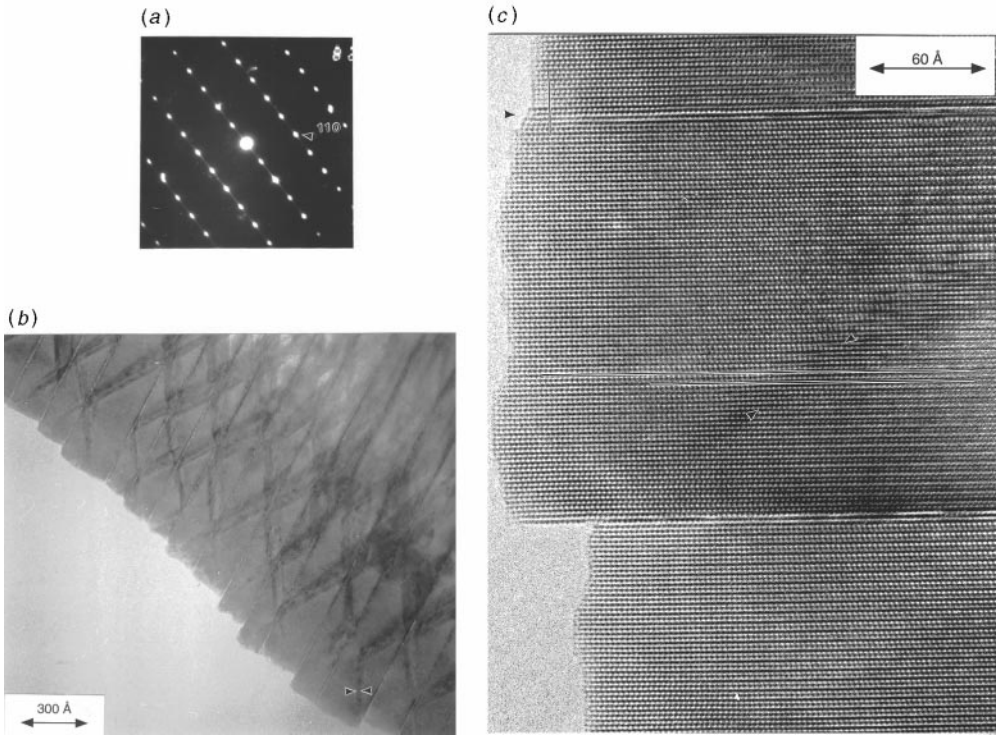

Fig. 3 (*a*) An electron diffraction pattern and (*b*) corresponding lattice image taken along [100] of a crystal found in a sample with nominal composition $InFeO_3(ZnO)_{23}$. The width of the bouncing defect at the arrows corresponds to a crystal thickness of 60 Å, see text. (*c*) Magnification of a part of the edge in (*b*). The shift of 0.9 Å along [100] when crossing the (001) defect (marked with an arrow) is emphasised with a line. The shift when crossing the bouncing defects (marked with arrows) is emphasised with two lines.

the (001) planes of the ZnO network. In the higher magnification one can see that the dark spots ascribed to zinc atoms at this defocus (*ca.* −400 Å) are shifted 0.9 Å along [120] when crossing this defect. This distance corresponds to a third of the height of a tetrahedral face.

The second type of defect was not always seen in the crystallites viewed along [100] or its equivalents. These defects have a more diffuse contrast, bouncing back and forth between the (001) defect layers forming zigzag patterns. In this projection ($\bar{2}10$), they have the shape of ribbons with more or less pronounced rims, increasing in width with the distance from the edge of the crystallites. (They appear as inclined layers when viewed along the [100] axis.) A shift of the contrast along the *c*-axis is observed in Fig. 3 when crossing a defect of the second type, which might be interpreted as a small shift of the zinc atoms along the *c*-axis. Weak streaking along the *c*-axis is seen in the corresponding ED patterns in Fig. 3(*a*), caused by the variation of the distance between the defects parallel to the (001) planes of ZnO. It has to be mentioned that anomalies of the same type were found in samples doped with less indium: $x=0$ and 0.5.

In order to determine the orientation of the defects in three dimensions, some crystallites were tilted 30° around the *c*-axis to the [$1\bar{1}0$] or the equivalent [210] directions. After this operation the bouncing defects were still seen in the HREM images in some cases, while in others they had disappeared. In both cases the first type of defect parallel to (001) remained clearly visible. An HREM image with bouncing defects visible in the new direction, and the corresponding electron diffraction pattern, are shown in Fig. 4.

In accordance with reports on highly doped compounds in this system,[19–21] we suggest that one half of the impurity atoms (indium or iron) are located in the plane defect layers. The number *m* of 'ZnO'-planes between the defect planes would then be $m=n+1$ [*n* from the formula $In_xFe_{2-x}O_3(ZnO)_n$]. As expected due to the short firing period, this number *m* varies markedly in the crystallites. However, the average of *m* for

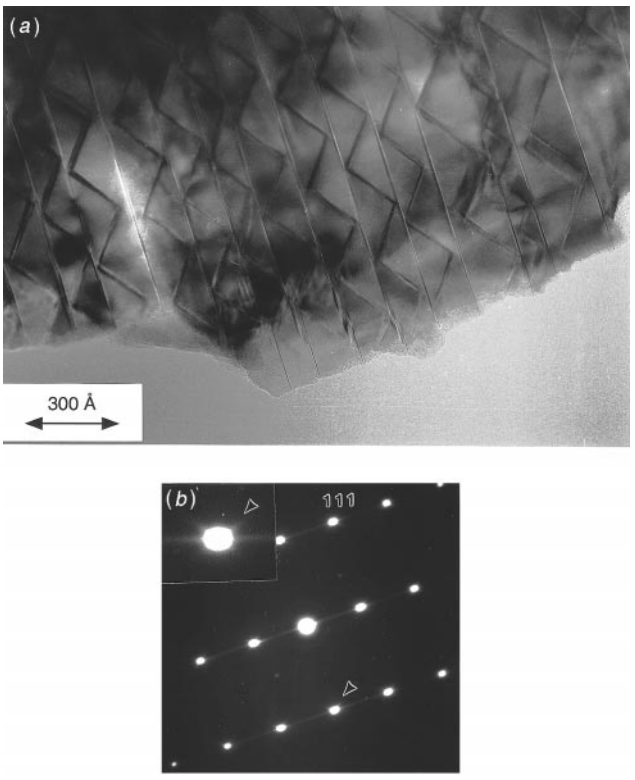

Fig. 4 (*a*) HREM image of a crystallite viewed along [$1\bar{1}0$] found in a sample with nominal composition $InFeO_3(ZnO)_{48}$. (*b*) The corresponding electron diffraction pattern, and magnification of a diffraction spot exhibiting a star of intensity along [114] and [$11\bar{4}$].

Table 1 Average distance between defect layers in the HREM images of crystallites studied in $In_xFe_{2-x}O_3(ZnO)_n$ samples, $m=n+1$

m	x	Observed m[a]
24	0.0	24
	0.5	30
	1.0	24
49	0.0	55
	1.0	51
99	1.0	90

[a]Approximate value.

the crystallites studied corresponds well with the amount of doping, as shown in Table 1. The planar defects seem to be very sturdy and without faults. This indicates that ordering towards a smaller spread in m is very sluggish; otherwise we would see that some layers were 'on the move' by showing steps. A fast structural rearrangement is not to be expected, since it must involve interchange of atoms.

When viewed along $[1\bar{1}0]$ or equivalent axes in ZnO, the shortest distances between zinc atoms in the projection are $c/2=2.60$ Å and $a/2=1.625$ Å. We can therefore only expect them to be resolved in the c direction. In the crystallite shown in Fig. 4(a), both types of extended defects are very clearly distinguished, the bouncing defects being more narrow and distinct in this projection than when viewed along [100]. This gives the impression that the defect planes are now oriented parallel to the beam. The angle between the two types of defect planes is approximately 39°. The estimated value of this angle does not vary much within different parts of the crystal or between different crystals. If we define the direction in ZnO where the bouncing defects are sharply visible to be $[1\bar{1}0]$, then the bouncing defects will be layers alternately parallel to (114) and $(11\bar{4})$. The angle between (114) or $(11\bar{4})$ and (001) planes in ZnO should be $\arctan(c/2a)\approx\arctan(1.60/2)\approx38.7°$, which is well in accord with the observed value.

In the ED-pattern taken along $[1\bar{1}0]$ there is streaking along the c axis as in the [100] patterns. The (114) or $(11\bar{4})$ boundary defects are also seen in Fig. 4(b) as a faint streaking in the shape of a weak star around the diffraction spots in the ED pattern. An enlargement of a diffraction spot is inserted in Fig. 4(b). The directions of the star points are close to the [114] and $[11\bar{4}]$ directions in reciprocal space, in agreement with the interpretation of the HREM images. The distinct 39° angle found between the planar defects and the bouncing defects when viewing along $[1\bar{1}0]$ decreases a few degrees, to *ca.* 35°, when viewing along [100], with a larger spread in observations. The preferred cleavage surface for ZnO is reported to be $(\bar{2}10)$.[25,26] It is therefore not unreasonable that the crystallites studied here are flakes extended in the equivalent $(\bar{2}10)$-planes—perpendicular to the [100]-axis. The angle between the defect types projected on a $(\bar{2}10)$-plane should be $\arctan[(c/2a)\cos(30°)]\approx34.72°$. The spread of observations is caused by the fact that the crystallites are wedge-shaped at the edges and increase in thickness with the distance from the edge, and they may not necessarily be exactly extended in the $(\bar{2}10)$-plane.

The structure of the bouncing defects together with the planar (001) defects very much resembles corrugated cardboard. The corrugated defect layers are not always seen, since in both viewing directions, [100] and $[1\bar{1}0]$, there are three equivalent cases in the hexagonal setting of the sublattice. In the first view along [100] the planes of corrugated defects make a 30° angle with the incident beam, but they may also be perpendicular to the incident beam and thus not seen. In the other projection, $[1\bar{1}0]$ and [210], the corrugated planes are either aligned with or 60° off the beam. In the latter case the angle may be too large to allow the observation of the defect layer. The angle between the corrugated layer and the electron beam will thus be either approximately 60 or 0°, and the bouncing defects will be visible in one case out of three.

Clearly this defect structure breaks the hexagonal wurtzite symmetry. We can therefore introduce an orthorhombic cell with reduced symmetry, related to the hexagonal wurtzite cell by:

$$\text{base(orth)}=\begin{pmatrix}1 & \bar{1} & 0\\ 1 & 1 & 0\\ 0 & 0 & 1\end{pmatrix}\text{base(hex)} \qquad (2)$$

This is of course a subcell of the structures that can occur in this system. However, for simplicity of description we will retain the hexagonal cell of ZnO.

The bounds of the ribbons formed by the bouncing defects, seen in the $(\bar{2}10)$ projection, are the intersections between the bouncing defect layers and the surfaces (top and bottom) of the crystal fragment. The width of the ribbons b is related to the thickness t of the crystal as $b=(t\sin\alpha)/\sqrt{3}$ ($\alpha=38.7°$, the angle between (114) and (001)), assuming the crystallites to be perpendicular to the beam. It is thus possible to determine the thickness of the crystals by measuring the width of the ribbons: for example the crystallite shown in Fig. 3(b) would then have a thickness $t\approx60$ Å at the position marked with the two arrows.

Our conclusions on the orientation of the defect planes are shown in a drawing. In Fig. 5(a) we look straight down on the (114) and $(11\bar{4})$ defects along $[1\bar{1}0]$ in ZnO. The resemblance to corrugated cardboard is striking. In Fig. 5(b) the model is tilted 30° with respect to in ZnO. The model is wedge-shaped from the edge (at the bottom) to the position marked with arrows, and then has constant thickness. The ribbons

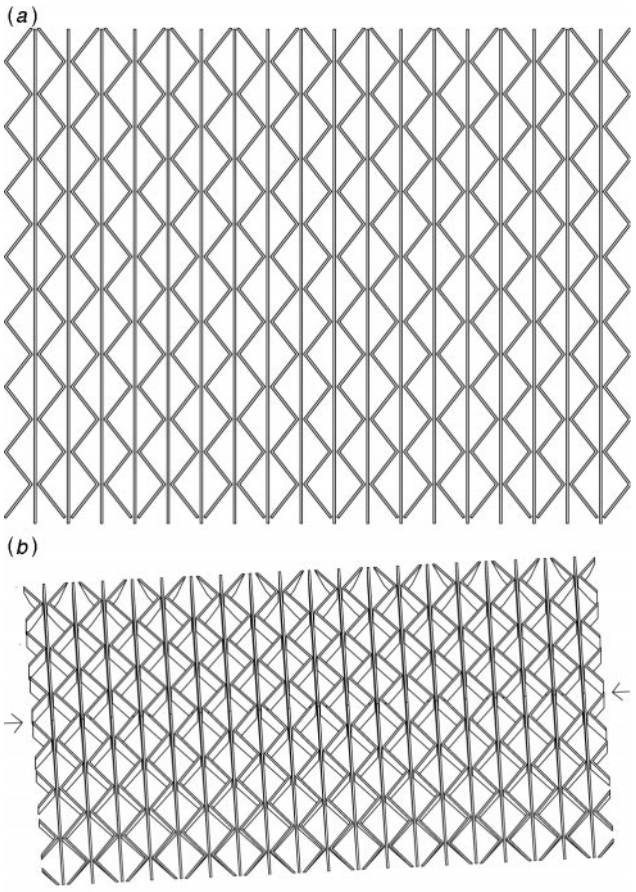

Fig. 5 Reconstruction of the (114), $(11\bar{4})$ and (001) defect planes. (a) Viewed along $[1\bar{1}0]$ and (b) along [100] in ZnO. The model is wedge-shaped from the edge to the position marked with arrows.

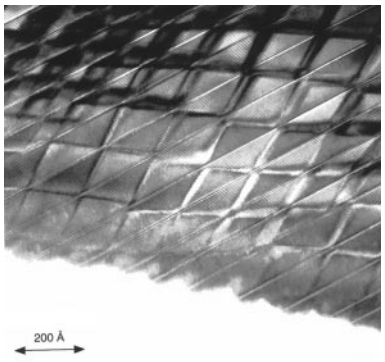

Fig. 6 HREM image of a crystallite found in a sample with nominal composition $In_{0.5}Fe_{1.5}O_3(ZnO)_{23}$, showing a well developed net of corrugated defects.

found in the HREM images are clearly seen in this orientation. Their width increases with the thickness of the 'crystal,' exactly as observed in the HREM images.

An impact of a corrugated layer on one side of a plane layer is frequently matched with an impact on the other side at almost the same place (exceptions occur). This means that the corrugated layers are mirrored through the planar layers, *i.e.* the waves of adjacent corrugated layers are 180° out of phase. The traces of the corrugated layers form a diamond net. This net is of course only well developed when there is some order in the *c* direction. Fig. 6 (of $In_{0.5}Fe_{1.5}O_3(ZnO)_{23}$ [100]) illustrates a rather well developed net with one planar and two corrugated layers are joined at each node. This is not always the case, as shown by the HREM image in Fig. 4(*a*), where both crossing and in-phase patterns are seen. There are also cases where corrugated defects turn before reaching the planar defect. The general appearance of our images is slightly different to that reported by Uchida *et al.* and by Bando and coworkers.[19–21] In the $(\bar{2}10)$ projection they observed sinusoidal contrast waves, in phase with each other and thus not forming a net. Uchida *et al.* also report the period lengths of the waves for two compositions [$InFeO_3(ZnO)_6$ and $InFeO_3(ZnO)_{13}$] in the $(\bar{2}10)$ and the $(1\bar{1}0)$ projection. They found the length shorter in the latter, which is consistent with our observations that the projected angle between the two types of defects is larger in the latter projection. The ratio between the lengths in the two projections is, however, not in accordance with our findings, and is not the same for the two compositions.

Analytical TEM

Spot analysis using EDX was performed on a crystallite oriented along [100], found in the $InFeO_3(ZnO)_{48}$ sample. We made point analyses of the planar defects, the bouncing defects and the intervening triangular ZnO parts. The beam size used was 10 Å. Although the low signal-to-noise ratio was unsatisfactory, the analysis gave a clear indication: indium prefers the planar defects while iron seems to be enriched in the bouncing defects in this compound. The result is in agreement with the report of Bando and coworkers.[19] To obtain a better signal-to-noise ratio we used EELS to perform elemental mapping. Two samples were investigated: (*i*) $Fe_2O_3(ZnO)_{48}$ and (*ii*) $InFeO_3(ZnO)_{48}$. The results confirmed the impression from the EDS analysis. A crystallite in the $Fe_2O_3(ZnO)_{48}$ sample was oriented along $[1\bar{1}0]$, of which an image using the zero beam is shown in Fig. 7(*a*). Two images using electrons that have lost energy due the K-absorption edges of iron and zinc are shown in Fig. 7(*b*) and (*c*). The iron map clearly shows that iron is enriched in the defects, and a corresponding dark contrast due to depletion of zinc in the planar defects is seen in the zinc map. To what extent there is iron in the ZnO slabs remains to be answered, but it seems probable that some iron is incorporated there. The sample just described did not contain indium, so a crystallite found in a sample with nominal composition $InFeO_3(ZnO)_{48}$ was investigated to locate this element and the zinc, indium and iron elemental maps are shown in Fig. 8. This crystallite is viewed along an equivalent to the $[1\bar{1}0]$, zone axis, in a direction where the bouncing defects are not viewed edge on, *e.g.* [210]. The indium map reveals a preference for the planar defects, whereas the iron and zinc signals indicate deficits in these defects. A uniform iron signal is found between the planar defects, as expected for a crystallite of finite thickness. The conclusions from this elemental mapping are (i) indium prefers the planar defect layer. Whether it is possible for indium to enter the corrugated layers is not clear. (ii) Iron may enter both types of defects.

Magnetic susceptibility

The magnetic susceptibility measurements revealed all doped samples to be paramagnetic. The diamagnetic contributions from zinc and oxygen have been removed in presented data. For this we used the measured susceptibility of ZnO, which was in excellent agreement with Pascal's constants tabulated in ref. 26. For the various species we expect the μ_B^2 to be 35 for Fe^{3+}, 24 for Fe^{2+} and 3 for electrons or In^{2+}, assuming spin-only contribution and high-spin configuration. (In oxides the ligand field is usually not strong enough to induce a low-spin state.) One may expect divalent indium and free electrons to be trapped by iron according to a prior study:[4]

$$In^{2+} + Fe^{3+} \rightarrow In^{3+} + Fe^{2+} \qquad e^- + Fe^{3+} \rightarrow Fe^{2+} \qquad (3)$$

There are two kinds of trivalent iron ions and a small fraction of divalent in the compounds studied. The squared effective Bohr magneton number per iron atom is shown in Fig. 9–11 for $n = 98$, 48 and 23 respectively. The curves marked A and B are from the samples with $x = 0.0$ and 1.0, respectively. The results of the analytical TEM show that iron is located in both types of defects when no indium is present ($x = 0.0$). For $x = 1.0$ the iron has a preference for the corrugated layers. A simple estimation of μ_{eff}^2 for iron in the planar defects can be calculated from

$$\mu_{eff}^2\,(C) = 2\mu_{eff}^2\,(x=0) - \mu_{eff}^2\,(x=1) \qquad (4)$$

which is shown in the curves marked C. At low temperatures the calculated value of the iron μ_{eff}^2 value in the planar defects becomes negative for two of the samples ($n = 23$ and 48). This indicates of course that the model represented by eqn. (4) is rather crude, but it can be used for a qualitative discussion. The low μ_{eff}^2 values, and the appearance of the curves in Fig. 9–11, clearly indicate an antiferromagnetic interaction between Fe^{3+} ions in both types of defect layers. This antiferromagnetic interaction is more pronounced in the planar defects. In a hexagonal layer of edge-sharing FeO_6 octahedra there are six nearest neighbours. Only four of these yield favourable antiferromagnetic interactions in an ordered structure, and the other two contacts will be unfavourable. In a hexagonal lattice there is no preference for the orientation of these interactions, but if the hexagonal symmetry is distorted this degeneracy is broken. The corrugated cardboard structure with orthorhombic symmetry may at least to some extent stabilise and orient an antiferromagnetic structure by giving a stronger interaction. The sharp bend of the C-curves at low temperatures may be an indication of a transition to a state where the magnetic structure of the planar defect is lined up with the corrugated layer structure.

Discussion

The structure of ZnO, wurtzite, can be described as a hexagonal close packing (hcp) of oxygen atoms, containing two different

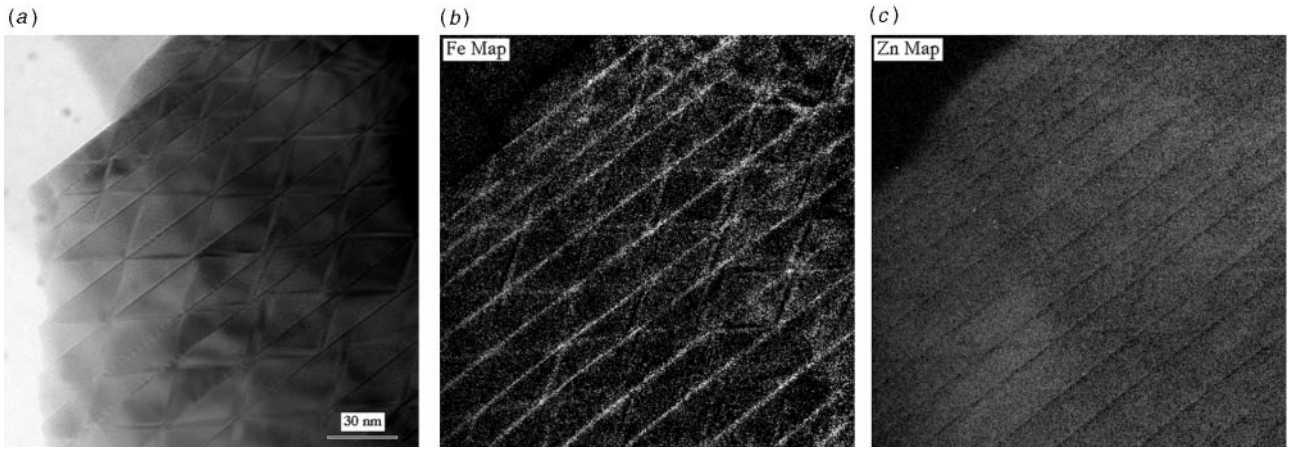

Fig. 7 Elemental distribution map, using EELS, of a crystallite in the $Fe_2O_3(ZnO)_{48}$ sample oriented along $[1\bar{1}0]$ to give the best contrast of the defects. (*a*) An image using the zero beam. The resolution is rather low due to the limitations of the EELS system, but the defects are clearly resolved. (*b*), (*c*) Images using electrons that have lost energy due to the (*b*) Fe-K absorption edges and (*c*) Zn-K absorption edges. The light contrast in the iron map clearly shows that iron is enriched in the defects, while a corresponding dark contrast due to deficiency is seen in the zinc map.

types of tetrahedral voids and one octahedral. The zinc atoms occupy only one type of the tetrahedral voids. The empty and the occupied tetrahedra share a basal plane, so as to form a trigonal bipyramid (in contrast to ccp). All the filled tetrahedra point their apices in the same direction, resulting in a polar structure. By shifting the zinc atoms through the equatorial plane of the bipyramids, the structure is mirrored and the polarity is reversed.

The (001)-plane defects in the doped structures are caused by insertion of an extra close-packed oxygen layer plus a reversal of the polarity of ZnO to one side. The result is that the apices of the ZnO_4 tetrahedra from each side of the (001) defects point towards each other without sharing oxygen atoms. The insertion of the extra close-packed layer is such that a portion of the oxygen layers are cubic close packed, and the voids with octahedral coordination are filled with trivalent ions. The formation of such a ccp slab shifts the zinc atoms in the ZnO layers on opposite sides through $a/2\sqrt{3}$ Å (*ca.* 0.9 Å) relative to each other. The indium and/or iron atoms are situated in octahedral cavities in these ccp layers. This model is in agreement with results of single-crystal studies of $LuFeO_3(ZnO)_n$ ($n=1$, 4, 5 and 6) reported by Isobe *et al.*[23] The directions of the shift of the zinc atoms on opposite sides of the ccp layers will depend on the number of 'ZnO' planes, $m=n+1$, between the defect planes, as observed in the HREM images. In the ordered structures an even number results in a

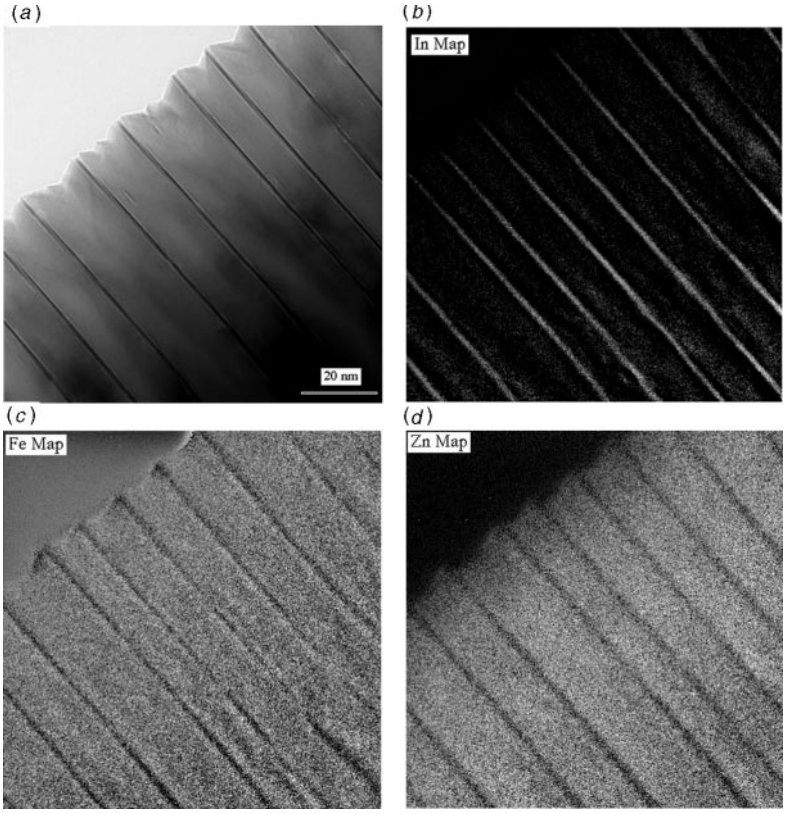

Fig. 8 Elemental distribution mapping, using EELS, of a crystallite oriented along $[1\bar{1}0]$ to give the best contrast of the defects found in a sample with nominal composition $InFeO_3(ZnO)_{48}$. (*a*) Zero-beam image. Images using electrons that have lost energy due to the (*b*) In-K absorption edges and (*c*) Fe-K absorption edges and (*d*) the Zn-K absorption edges. The orientation of the crystallite is such that the bouncing defects are inclined to the beam. The image shows that indium prefers the planar defects, which are avoided by the zinc and iron atoms.

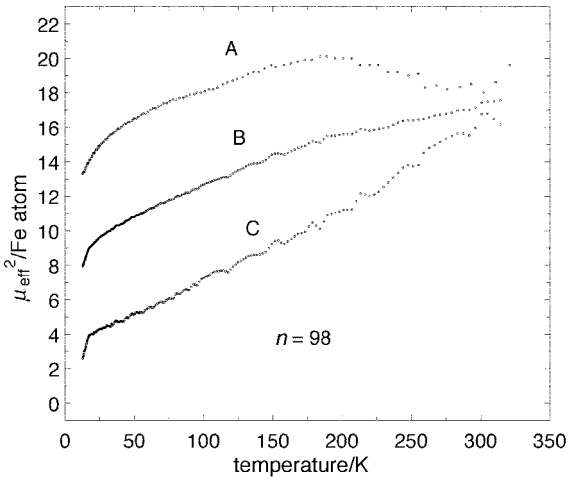

Fig. 9 The squared effective Bohr magneton number per iron ion for $n=98$. A, The value for the samples $x=0.0$ with iron in both types of layer defects. B, The contribution from samples $x=1.0$ with iron atoms only in the bouncing defect layers, since there is indium in the planar defects. C, The magnetic moment from iron in the planar defects is calculated from eqn. (4) in the text.

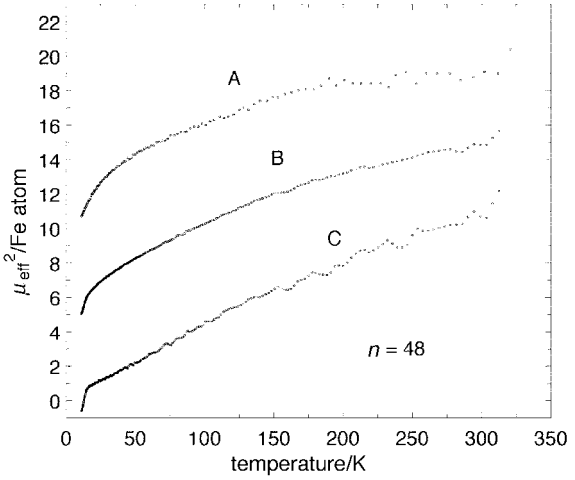

Fig. 10 The squared effective Bohr magneton number per iron ion for $n=48$. A, The value for the samples $x=0.0$ with iron in both types of layer defects. B, The contribution from samples $x=1.0$ with iron atoms only in the bouncing defect layers, since there is indium in the planar defects. C, The magnetic moment from iron in the planar defects is calculated from eqn. (4) in the text.

hexagonal space group, $P6/3mcm$, while odd numbers yield the rhombohedral symmetry $\overline{R}3m$, see Appendix. We have simulated HREM images of the ccp layers, using the coordinates from the ordered structures with $n=5$ and 6. These show good agreement with our observed HREM images and also with published calculated and observed images.[21] The difference between the simulated images having indium or iron in the ccp layers is rather small.

As mentioned above, the ZnO_4 tetrahedra are always oriented with their apices towards the ccp layers. If the polarity were to be reversed by letting three oxygen atoms of the ZnO_4 tetrahedra be shared by the octahedra, then the metal ions would come to close to each other. The polar axis of the ZnO slabs thus must change direction somewhere between the ccp layers. The single-crystal structure studies[23] of the ordered lutetium-containing compounds $[LuFeO_3(ZnO)_n]$ with small n values, $n\leqslant 6$, show that this change of polarity is accommodated by a gradual shift of the metal atoms from one tetrahedron to the neighbouring empty one. As a result the metal atoms have trigonal bipyramidal coordination halfway between the ccp layers. The detailed crystal structure analysis

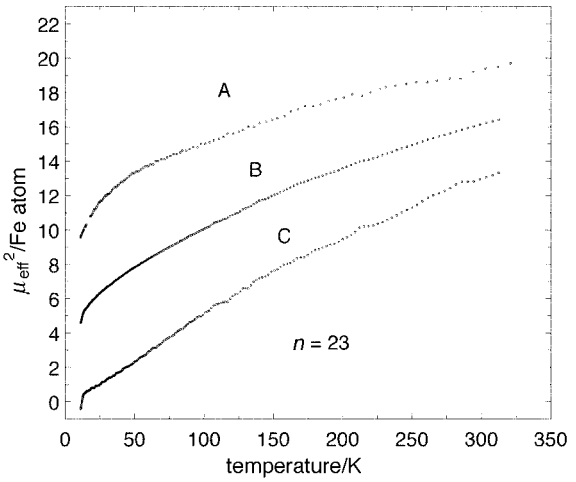

Fig. 11 The squared effective Bohr magneton number per iron ion for $n=23$. A, The value for the samples $x=0.0$ with iron in both types of layer defects. B, The contribution from samples $x=1.0$ with iron atoms only in the bouncing defect layers, since there is indium in the planar defects. C, The magnetic moment from iron in the planar defects is calculated from eqn. (4) in the text.

of these compounds revealed no preference of iron for the layer of trigonal prisms halfway between the ccp layers. (One would expect the zinc atoms to avoid the trigonal bipyramidal positions, as this co-ordination is very unusual for zinc, while there are some compounds known with iron in trigonal bipyramids, see *e.g.* ref. 28. The lutetium atoms were found in the ccp layers, as expected.

As already mentioned, Uchida *et al.*[21] observed the wave structures discussed above when investigating $InFeO_3(ZnO)_n$ ($n\leqslant 6$), but they did not present any structural explanation for the phenomenon. If similar waves also occur in the structure of the lutetium compound with $n=6$, which was determined by single crystal diffraction, it could explain why no preference for the trigonal bipyramids was found for iron. The single-crystal studies give the average structure, and this partly disordered modulation therefore cannot be seen. As a consequence, there are not necessarily any perfect (001) layers of trigonal bipyramids half-way between the (001) layers when $n>0$.

In dilute structures, $n>6$, most of the material is ZnO which naturally relaxes to the wurtzite structure. Therefore the reversal of polarity must be confined to rather narrow ranges, less than the width of the slabs between the planar defect layers. The corrugated layers may contain such a transition. It is difficult, however, to explain why such a domain boundary should be locked to certain crystallographic planes (114) or $(11\bar{4})$ if the transition is gradual. Moreover, a gradual transition does not fit in with the fact that the electric charges are local. The charge required for polarity reversal is provided by proper localisation of trivalent iron. This idea is supported by the observation that the iron is enriched in the bouncing defects. It is very reasonable to anticipate that the these defects cause the shift in polarity in ZnO necessary to fit the ccp layers. The small shift in contrast in the HREM images when crossing these bouncing defect layers corroborates this idea, see Fig. 3. Since these structures are disordered, detailed information cannot be obtained by using X-ray diffraction techniques. Still, there is some information that can be used to construct a structural model for the defects:

(i) There is a difference in polarity between the ZnO slabs on opposite sides of the ccp layers. Consequently there has to be a reversal of polarity somewhere between these layers.

(ii) There must be reasonable charge balances, interatomic distances and coordination spheres around the atoms. Fe^{3+}

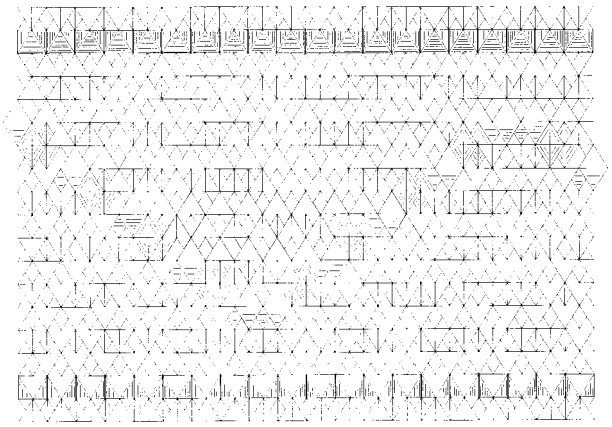

Fig. 12 A structural model showing the bouncing defects as formed by trigonal bipyramids viewed along [1$\bar{1}$0].

can occupy tetrahedra, trigonal bipyramids and octahedra, whereas Zn^{2+} prefers tetrahedra.

(iii) EDS and EELS investigations clearly show an enrichment of indium or iron in the ccp layers and of iron in the bouncing defect layers ((114) and (11$\bar{4}$) planes).

(iv) Magnetic data show a coupling between the iron atoms. They are located close to each other in both types of defects (if not diluted by indium in the (001) defect).

(v) The defects are narrow and distinct in the crystallites viewed along [1$\bar{1}$0].

In accordance with the list above, two structural models have been constructed to describe the bouncing defect layers. In the first model we suggest that the change in polarity occurs *via* double chains of trigonal bipyramids, with trivalent ions in the equatorial plane. These chains run along [1$\bar{1}$0] and are linked to form planes parallel to (114) and (11$\bar{4}$) in ZnO. This structural model viewed along [1$\bar{1}$0] is shown in Fig. 12. The second model comprises a movement of the cations from the equatorial positions in the bipyramids to neighbouring octahedral cavities. The latter model is shown in Fig. 13. The octahedra share edges as in α-PbO_2, forming chains along [1$\bar{1}$0] in (114) and (11$\bar{4}$) planes in ZnO. None of the models includes large movements of the oxygen atoms. The hcp net of oxygen atoms is in principle preserved, and only the cations are moved. These two models conform to the list of observations and requirements above and are simple enough to be tangible, but it is not obvious which is the correct one, if any. One may also consider the possibility that the first, with bipyramids, is appropriate for lower *n*-values and that the second, with octahedra, for higher *n*-values. The most important argument for the octahedral model is that there are rather few oxides known with iron in trigonal bipyramidal coordination except the lutetium compounds.[23] One such compound is $InFeO_3$.[28] To finally settle which model is correct, one of our suggestions or some other, additional information is needed from, for example EXAFS and Mössbauer studies.

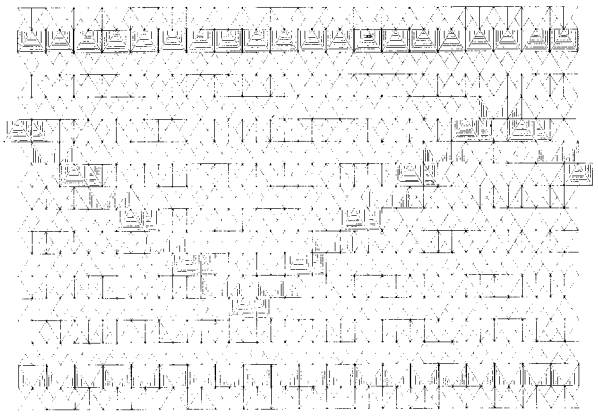

Fig. 13 A structural model showing the bouncing defects as formed by α-PbO_2 type chains of octahedra viewed along [1$\bar{1}$0].

Appendix

The common chemical formula for these types of compounds is: $MM'O_3(ZnO)_n$ where M is the metal residing in the plane defect layers (marked below with dots in the layer sequences).

In the ordered compounds there are then $n+3$ close packed oxygen layers within each subperiod (distance between the plane defect layers).

If *n* is an integer there are two cases:

(i) *n* is odd and the sequence of oxygen layers is:

$$\begin{array}{c} |\,\text{subperiod}\,| \\ \bullet(\text{A B})^k\bullet(\text{C A})^k\bullet(\text{B C})^k\bullet(\text{A B})^k\bullet(\text{C A})^k\bullet \\ |\quad\text{period}\quad| \end{array}$$

Here: $k=(n+3)/2$ and period $=3\times$ subperiod;

the symmetry is trigonal;

(ii) *n* is even and the sequence of oxygen layers is:

$$\begin{array}{c} |\ \text{subperiod}\ | \\ \bullet(\text{A B})^k\,\text{A}\bullet(\text{C B})^k\,\text{C}\bullet(\text{A B})^k\,\text{A}\bullet(\text{C B})^k\,\text{C}\bullet \\ |\quad\text{period}\quad| \end{array}$$

Here: $k=(n+2)/2$ and period $=2\times$ subperiod;

the symmetry is hexagonal.

This work originates as a spin-off from a multi-national industrial project concerning high-temperature electrode materials. In the Northern countries it was co-ordinated by Michael Hatcher at 'Permascand'. Our work was later supported by NUTEK (Swedish Board for Industrial and Technical Development) and NFR (Swedish Natural Science Research Council). We are in debt to the participants in the early stages of this work: Mats Nygren, Jekabs Grins, and the late Thomasz Niklewski.

References

1 G.Heiland, E.Mollwo and F.Stöckmann, *Solid State Phys*., 1959, **8,** 193.
2 R. Wang, A. W. Sleight and D. Cleary, *Chem. Mater.*, 1996, **8**, 433.
3 R. Wang, A. W. Sleight, R. Platzer and J. A. Gardner, *J. Solid State Chem.*, 1996, **122**, 166.
4 T. Hörlin and J. Grins, unpublished results.
5 H. Kasper, *Z. Anorg. Allg. Chem*. 1967, **349,** 113.
6 P. J. Cannard and R. J. D.Tilley, *J. Solid State Chem*., 1988, **73**, 418.
7 M. A. McCoy, R. W. Grimes and W. E. Lee, *Philos. Mag. A*, 1997, **76**, 1187.
8 N. Kimizuka, T. Mohri, Y. Matsui and K. Siratori, *J. Solid State Chem*., 1988, **74,** 98.
9 M. Nakamura, N. Kimizuka and T. Mohri, *J. Solid State Chem*., 1990, **86,** 16.
10 N. Kimizuka, M. Isobe, M. Nakamura and T. Mohri, *J. Solid State Chem*., 1993, **103,** 394.
11 N. Kimizuka and T. Mohri, *J. Solid State Chem*., 1989, **78,** 98.
12 M. Nakamura, N. Kimizuka and T. Mohri, *J. Solid State Chem*., 1991, **93,** 298.
13 K. Siratori and N. Kimizuka, *J. Solid State Chem*., 1992, **99,** 243.
14 M. Nakamura, N. Kimizuka, T. Mohri and M. Isobe, *J. Solid State Chem*., 1993, **105,** 535.
15 M. Nakamura, N. Kimizuka, T. Mohri and M. Isobe, *J. Alloys Comp.*, 1993, **192,** 105.

16 T. Tsubota, M. Ohtaki, K. Eguchi and H. Arai, *J. Mater. Chem*., 1997, **7,** 85.
17 H. Ohta, W-S. Seo and K. Koumoto, *J. Am. Ceram. Soc.*, 1996, **79**, 2193.
18 N. Kimizuka, M. Isobe and M. Nakamura, *J. Solid State Chem*., 1995, **116,** 170.
19 N. Uchida, Y. Bando and N. Kimizuka, *13th Int. Conf. Electron. Microsc.*, *Paris*, 1994, vol. 2, p. 891.
20 Y. Bando, *13th Int. Conf. Electron. Microsc. Paris*, 1994, vol. 1, p. 591.
21 N. Uchida, Y. Bando, M. Nakamura and N. Kimizuka, *J. Electron Microsc*., 1994, **43,** 146.
22 E. Olsson, G. Svensson and T. Hörlin, *Eur. Meet. Electron. Micr. Dublin*, 1996.
23 M. Isobe, N. Kimizuka, M. Nakamura and T. Mohri, *Acta Crystallogr.*, *Sect. C*, 1994, **50**, 332.
24 K. E. Johansson, T. Palm and P.-E. Werner, *J.Phys. E*, 1980, **13**, 1289.
25 V. D. Frechette and C. F. Cline, *Am. Mineral*., 1963, **48**, 1381.
26 R. A. Powell, W. E. Spicer and J. C. McMenamin, *Phys. Rev. B*, 1972, **6**, 3065.
27 F. E. Mabbs and D. J. Machin, *Magnetism and Transition Metal Complexes*, Chapman and Hall, London, 1973.
28 D. M. Giaquinta, W. M. Davis and H.-C. Zur Loye, *Acta Crystallogr.*, *Sect. C*, 1994, **50**, 5.

Paper 8/05291C